RESEARCH

LEGO calibration targets for large-FOV particle image velocimetry

Agastya Parikh[1] · Thomas Fuchs[1] · Matthew Bross[1] · Christian J. Kähler[1]

Abstract

Particle image or particle–tracking velocimetry nonintrusively provides velocity field information, and the proposition large field-of-view (FOV) measurements are highly attractive from an experimental standpoint. Stitching multiple smaller FOVs to achieve the large FOV of interest is an approach that faces challenges rooted in the calibration process. For stereoscopic PIV (SPIV), the use of a multi-level target simplifies calibration. However, this is problematic for large-FOV measurements, as standardised multi-level targets are relatively small and expensive. LEGO® bricks are well-suited to the construction of large, customised multi-level targets due to their high-dimensional tolerance and their stackability with high precision. To evaluate the feasibility of LEGO®-based targets, a two-sided multi-level target covering 380×1150 mm was created and used for SPIV measurements of the inflow conditions of the Atmospheric Wind Tunnel Munich. Calibrations were also performed using the Type 31 target for comparison. Analysis of the datasets with both calibration targets shows good agreement in the measurement of the streamwise, out-of-plane component u. A parametric study of different LEGO® target configurations was used to verify the calibration performance of the targets as well as identify optimal configurations for experimental use. Due to the high level of agreement in calibration parameters and quantitative and qualitative flowfield parameters in PIV tests, as well as the consistency observed in the subsequent parametric study, LEGO-based calibration targets show potential for further development and usage in large-FOV measurements.

Graphic abstract
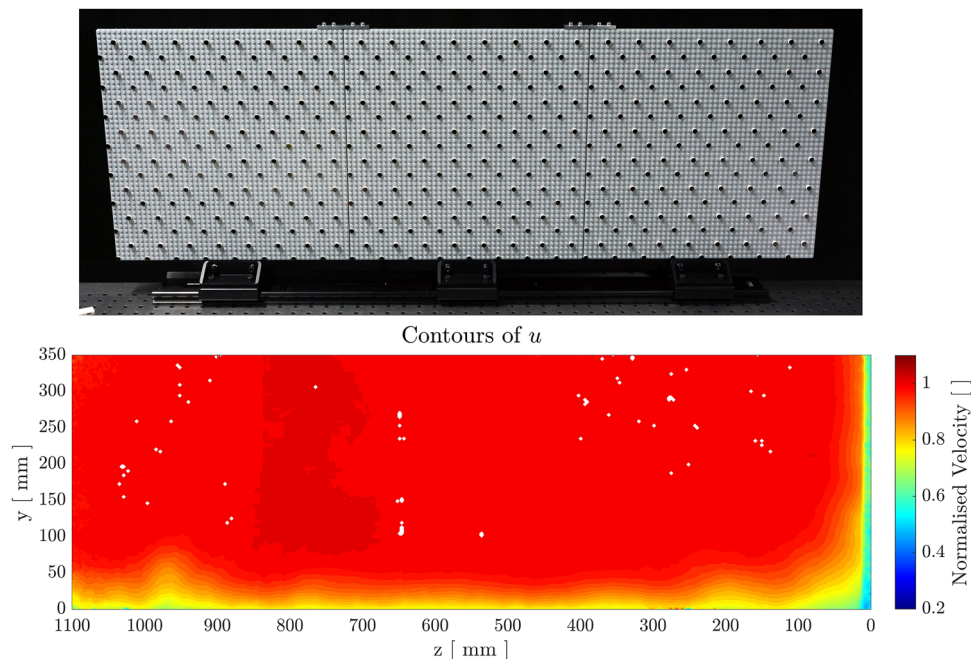
1 Introduction

One of the great benefits of particle image or particle-tracking velocimetry (PIV/PTV) as an experimental technique is that it nonintrusively provides velocity field information. Consequently, the proposition of measurements in a large plane is highly attractive from an experimental standpoint, particularly for experiments conducted in large atmospheric and flight-scale wind tunnels. Of course, there are physical limits to the size of the useful field-of-view (FOV) that can be achieved with a single camera (or a pair, in the case of stereoscopic measurements). These are often imposed by requirements on particle image size or desired resolution, which depend on striking a balance between the physical capabilities of the cameras and the physics of interest in the flow (Raffel et al. 2018; Scharnowski and Kähler 2020). A typical solution is to stitch together measurements in multiple smaller FOVs to provide data for the large FOV of interest.

Such large composite FOVs present a number of challenges, some of which are rooted in the calibration and alignment of the imaging system. Stitching imaged FOVs prior to cross-correlation rather than *a posteriori* stitching of vector fields is a common approach (Cardesa et al. 2012). For this, the smaller FOVs should first be calibrated individually in order to reduce the effects of optical aberrations, and then be stitched together using common reference points, ideally based on a common calibration target (Li et al. 2021). As stitching involves the use of the edges of the imaged area, where optical aberrations are the strongest, the use of a polynomial calibration is preferred to the simpler pinhole model (Cardesa et al. 2012; Raffel et al. 2018; McKeon et al. 2007). For proper use of polynomial mapping functions, the calibration target must provide a high degree of coverage of the imaged area (Cardesa et al. 2012; Li et al. 2021). This presents a drawback, as targets must now be customised to fit the experiment being conducted without sacrificing precision (Li et al. 2021). Furthermore, this becomes even more difficult for stereoscopic PIV (SPIV) measurements, where calibration must be performed with the target precisely positioned at various out-of-plane locations (Jenkins et al. 2009; Raffel et al. 2018). As the desired size of the composite FOV grows, so does the difficulty of positioning an equally large calibration target. A procedurally simpler alternative to displacement-based calibration for SPIV is the use of a multi-level target, where some calibration markers are offset by a precise distance in the out-of-plane direction to emulate translation (Raffel et al. 2018; Wieneke 2005). However, this is problematic from a customisation standpoint, as standardised multi-level targets are typically relatively small, expensive, and precision-engineered.

Therefore, the challenge with calibrating for multi-camera large-FOV measurements can be reduced to that of a suitably large calibration target which retains the physical precision necessary for accurate calculation of de-warping functions without being prohibitively complex or expensive. Detection of the marker pattern on a calibration target imposes a few basic requirements, chief among them being that the markers provide sufficient contrast against their background and that they are of a regular shape and size. Due to the need for high contrast, opaque calibration targets typically have a white-on-black or black-on-white colour scheme. To provide size regularity and ease of detection at various viewing angles, the markers are usually circular or cruciform in shape (Raffel et al. 2018).

LEGO® bricks are extremely well-suited to this purpose; they have a stated injection-moulding dimensional tolerance of 0.004 mm, and their stackability with high precision offers the dimensional stability needed for the construction of a multi-level SPIV calibration target (The LEGO Group 2018). Furthermore, flat circular tiles of various sizes are readily available within the LEGO® System, allowing for adaptation to different combinations of working distances, FOV, and imaged pixel sizes. This is of particular importance as markers which have a too small of an imaged size will appear pixelated, increasing the discretisation error in the calibration procedure. Conversely, overly large markers reduce the number of points available for accurate determination of the image de-warping function applied during calibration. An additional benefit is that LEGO® baseplates are available in large sizes, up to $38 \times 38 \text{ cm}^2$, and can easily be connected to each other to create larger target platforms in a modular manner.

2 Calibration markers

For LEGO® tiles to appear as planar markers to the cameras, their upper surfaces have to be coated while leaving the sides unmodified. Therefore, white tiles modified to have black upper surfaces were chosen for use on light-coloured baseplates. Several methods were considered for this modification; here, both the practicalities of the method of modification and its efficacy were important. The need for a high level of regularity in coating coverage, quality, and thickness across hundreds of marker tiles dictated the treatment of a large surface area in a relatively short period without the use of a complex labour-intensive process. Consequently, the application of paint and ink was the two primary surface colouring methods considered.

Although spray painting appears to be an obvious coating solution, restricting paint coverage to the upper surface of the tiles would require labour-intensive masking of the sides of each tile. Brush-based paint application does not

produce uniform layers, so a stiff rubber paint roller was chosen instead. With this, a thin layer of paint could rapidly be applied to multiple marker tiles simultaneously. Ink could either be applied without excessive labour using a broad-tipped marker or with an inkpad. Initial tests with a standard stamp inkpad showed that the ink beaded up and did not adhere well to marker tile surfaces.

Consequently, matte black model paint was successfully applied with a stiff rubber paint roller. Ink applied with a broad-tipped permanent marker showed good adhesion and uniformity when allowed to dry for a short period between coats. For both paint and ink, dripping of excess colouring agent over the sides of the marker tiles during application was a concern, but this could be mitigated with careful application. As matte surface finishes are often used in optical applications to reduce glare and specular reflections, some variants of the two surface colouring methods were tested as well. One painted tile was rubbed with isopropanol to create a more matte finish; this approach was also used with a tile coated by a permanent marker. Finally, one tile was roughened prior to being coated with permanent marker. Consequently, the only glossy tiles tested were an unmodified white tile and a tile coloured with a permanent marker.

The effectiveness of the surface modification was evaluated in terms of the achievable intensity ratio at viewing angles of 0°, 30°, and 45°, which bound typical 2D2C PIV and 2D3C SPIV viewing angles. For this, a single 2×2 tile marker was placed on a baseplate and illuminated directly by an LED light array and photographed with a Canon EOS 450D at a 0° working distance of approximately 0.7 m. The images were analysed in terms of the apparent light intensity using DaVis 10. As shown in Fig. 1, the achievable contrast between the marker and the background varied significantly with both surface coating and viewing angle. Qualitatively, it is apparent that increasing viewing angle resulted in increased contrast between the marker tile and the baseplate, regardless of the surface modification used. Notably, the tile coloured using permanent marker alone produced markedly more contrast than the others at the 0° and 30° viewing angles. Of additional interest is that both tiles with a paint coating showed relatively good uniformity, while only the unmodified permanent marker coating produced a consistently homogeneous intensity across the marker surface.

In order to quantitatively identify the most effective coating, as well as the influence of baseplate colour on achievable intensity ratio, area-averaged light intensities were calculated in DaVis as shown in Fig. 2. These data were then used to calculate the intensity ratio, defined as
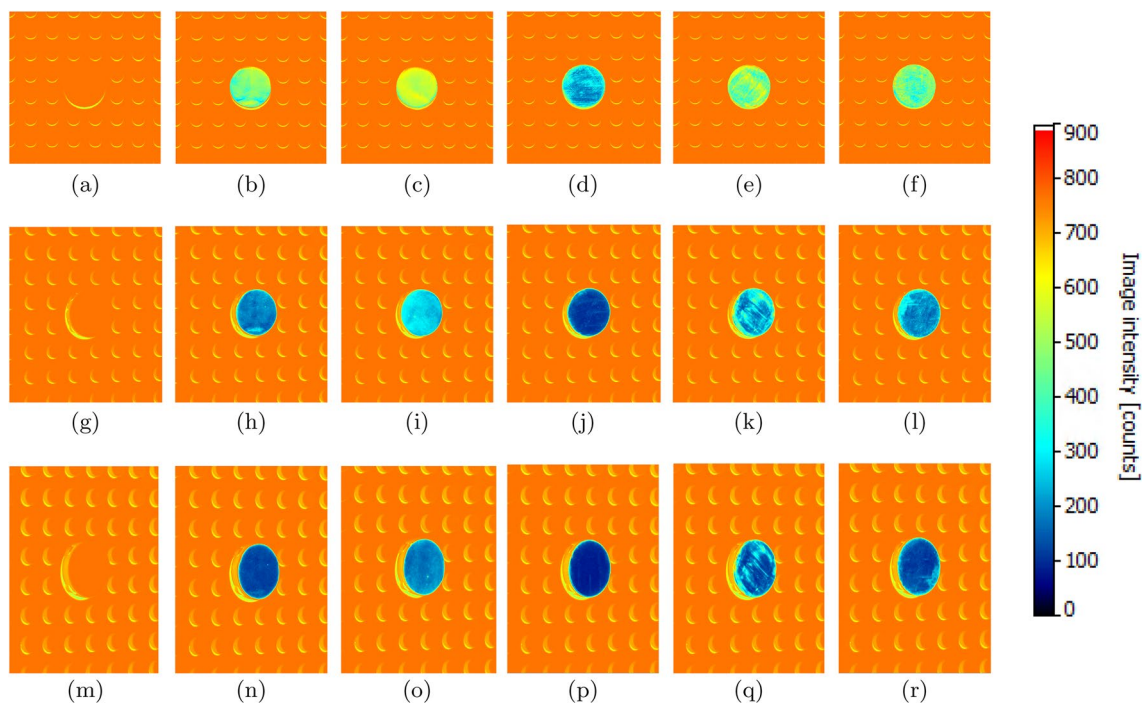

Fig. 1 Images used for intensity ratio measurement of marker tiles with various surface treatments at different viewing angles, coloured by intensity. Shown in each row (in order) are tiles treated with no coating, matte paint, matte paint with isopropanol, permanent marker, permanent marker with isopropanol, and sandpaper with permanent marker. The first row (**a–f**) is at a viewing angle of 0°, the second (**g–l**) is at 30°, and the third (**m–r**) is at 45°
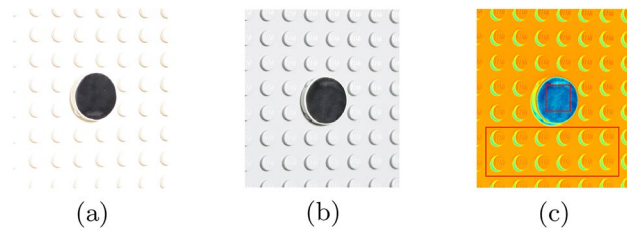
Fig. 2 Colour images of a paint-coated marker viewed at 30° against white (**a**) and grey (**b**) backgrounds. **c** shows **b** coloured by intensity and the interrogation rectangles (in red) used to compute mean intensity values for the marker and background. Note that due to perspective shifts, the exact geometry of the rectangles was adapted to the viewing angle
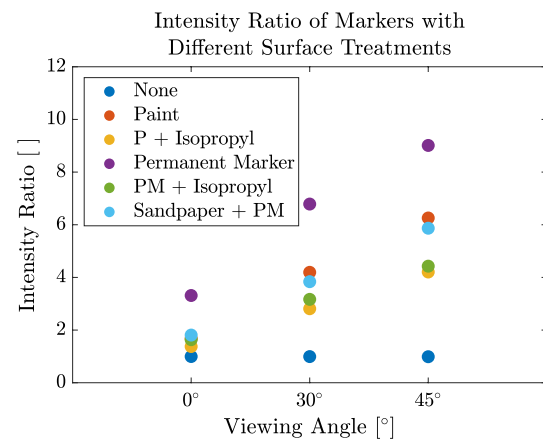
$$\mathrm{IR} = \frac{\langle I_{\mathrm{background}} \rangle}{\langle I_{\mathrm{marker}} \rangle} \qquad (1)$$

The intensity ratios for each combination of marker and viewing angle are shown for the white baseplate in Fig. 3a and the grey baseplate in Fig. 3b. For both background colours, the tiles coated with permanent marker alone yield the greatest contrast. Interestingly, the permanent marker-coated tile produces a greater contrast against the background of a grey baseplate for both the stereoscopic viewing angles in the dataset. Although it is somewhat contrary to the expected result, as the white baseplate was expected to provide superior contrast, this result is encouraging as it supports the use of the larger grey baseplates for target construction.

3 Multi-level LEGO® targets

In order to create a prototype multi-level SPIV target and evaluate whether the markers could provide sufficient contrast for pattern detection, even in the presence of shadows, the LaVision Type 31 target was chosen as a model. This target has a multi-level white-on-black marker pattern, with a dot diameter of 3 mm, marker pitch of 15 mm, and level displacement of 3 mm. For LEGO® bricks, the range of available patterns is somewhat dictated by the stud pattern. Stud pitch is 8 mm, which allows for a minimum marker pitch of 16 mm, where every alternate stud has a marker tile placed on it. 1 × 1 tile diameter is 7.8 mm, and one 1/3 height plate provides a planar separation of 3.2 mm. Although the minimum marker pitch and interplanar distances are quite similar to the Type 31 target, marker diameter is significantly greater. However, this plays less of a role, as markers are reduced to their centre points for calibration purposes.

Due to the rather similar geometries possible with the LEGO® bricks, a simple 3 × 3 two-level pattern and an analogous pattern with twice the marker pitch were imaged and compared to a 3 × 3 crop of the Type 31
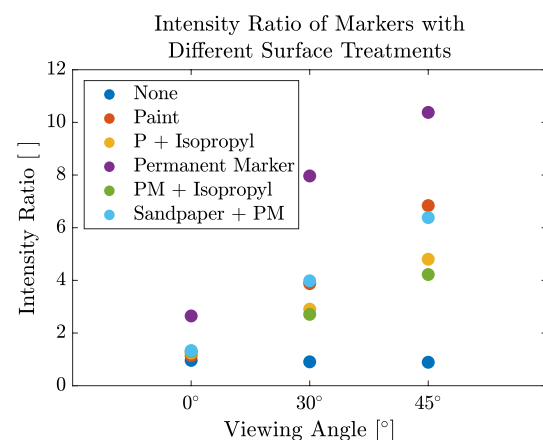
Fig. 3 Marker-background intensity ratios for different marker coatings and at different viewing angles, for a white baseplate (**a**), and a grey baseplate (**b**)

target; a faux-Type 31 and wider-spaced brick pattern could be identified by DaVis for calibration. Due to the rather similar geometries possible with the LEGO® bricks, a simple 3 × 3 two-level pattern approximately the same size as the Type 31 pattern was produced. This was imaged and compared to a crop of the Type 31 target; both patterns could be identified by DaVis for calibration. A limitation of this test was that the physical area covered by the target patterns was relatively small. Consequently, illumination intensity was fairly consistent across the imaged area, yielding near-ideal intensity ratios. As calibration targets increase in size, it becomes challenging to provide uniformly intense illumination across the entire area, and the detection of poorly illuminated calibration markers near the edges of a FOV can be problematic, even with professionally produced targets. As an initial test in actual measurement conditions, a large multi-level target composed of two 38 cm baseplates with a marker pitch of

48 mm was created. The baseplates were mounted side-by-side to a planar medium-density fibreboard (MDF) plate. In the experiment performed, a heated dummy was placed on a chair to investigate the buoyancy effects of bodily heat output. The laser sheet was located in a floor-parallel plane 30 cm above the head of the dummy; the cameras were oriented such that they were looking upwards from the floor at the measurement plane. This imaging configuration with stereoscopic viewing from one side of the laser sheet allowed for the use of a one-sided two-level pattern on the targets. Calibration using the pinhole method was successful under realistic experimental conditions, and the target could then be used for the measurements which are described in Sankaran et al (Tsai 1986; Sankaran et al. 2022).

With these results serving as validation of the basic feasibility of LEGO®-based multi-level calibration targets, two-sided two-level calibration targets fully analogous to the LaVision Type 31 were designed to be used during a pre-planned experimental campaign to measure the inflow conditions of the Atmospheric Wind Tunnel Munich (AWM). As the tunnel has a large cross-section of $1.85 \times 1.85 \ m^2$, and the objective is to evaluate flow conditions over >50% of its area using SPIV, the use of a large calibration target was ideal. In order to further augment the flexibility offered by the LEGO®-based targets, the backing used to mount the baseplates was designed to be modularly reconfigurable, offering the ability to create differently mounted or differently shaped rectilinear targets. This decision to use smaller constituent "sub-targets" rather than a single monolithic target had the further benefit of allowing for the use of tighter tolerances within ISO manufacturing standards when producing the target backing plates.

The target backing plates shown in Fig. 4 were CNC machined from Aluminium 6061. As is visible, they were designed with cut-outs in order to reduce their weight to minimise deformation when mounted in a cantilevered configuration; they can be mounted using a pair of M6 bolts using the tab on one of the four sides, with the remaining three sides being available for modular combination with other targets. 4 mm alignment pins and alignment rails attached with M4 screws are used to connect different target backing plates to each other. After machining, they were coated with RAL9005 matte black paint to minimise any potential reflections on exposed surfaces during calibration imaging. Each of the "sub-targets" was assembled independently before being connected to create the final two-sided, multi-level large-FOV target shown in Fig. 4c. It is important to note that the "sub-targets" can be mated along 3 of their edges with no limitation on their number, to create a variety of target sizes and shapes to fit different experimental needs.
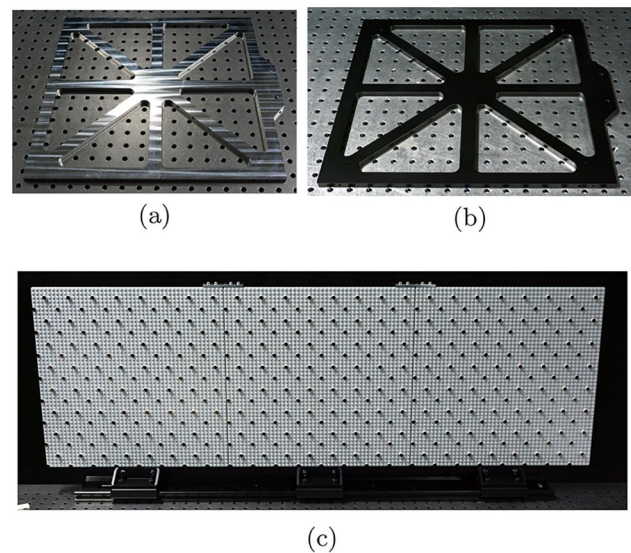

Fig. 4 Target backing plates, immediately after CNC machining (**a**), and after coating with anti-reflective paint (**b**). The complete two-sided, multi-level LEGO® target (**c**) measures approximately 380 × 1150 mm

4 Large-FOV stereoscopic PIV experiments

Measurement of the inflow conditions of the AWM required optical coverage of a large area, with the final half-plane being composed of the data from smaller FOVs, each roughly corresponding in size to the large-FOV target. To image these smaller constituent FOVs, three individual SPIV systems were synchronised to simultaneously image overlapping regions. In all, six Imager sCMOS cameras with a sensor size of 2560×2160 px were equipped with $f = 100$ mm Zeiss ZF Makro-Planar lenses. As shown in Fig. 5, the cameras were stacked in order to image a vertically oriented FOV at a working distance of approximately 2.3 m, measured from the centre of the calibration target. The FOV of each pair of cameras has an approximate usable area of 500 × 350 mm, with the longer dimension being in the spanwise direction.

An Innolas Spitlight 1000-15 Nd:YAG dual-head pulsed laser was used to generate the light sheet. To reduce the intensity of reflections at the wall and minimise the associated data loss in the region, the light sheet was oriented tangentially to the side wall of the wind tunnel. The laser has a fixed repetition rate of 15 Hz, at which 950 images were taken for each dataset to provide sufficiently converged data to calculate turbulent statistics. Seeding particles were generated using a Di-Ethyl-Hexyl-Sebacate (DEHS) particle generator placed in the inlet tower of the AWM. This is sufficiently far upstream to produce homogeneous seeding in the imaged area. To obtain data representative of the typical operational range of the tunnel, measurements were
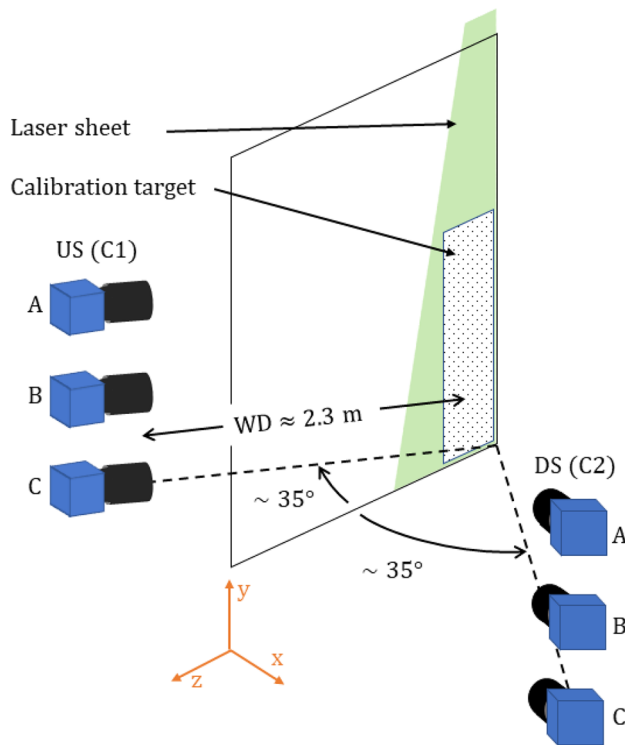
Fig. 5 A quasi-3D schematic of the SPIV set-up used. The cross-section of the AWM is outlined in black, and the approximate position of the cameras and calibration target is shown. The upstream (US) cameras and downstream (DS) cameras are organised into 3 separate SPIV set-ups, labelled A, B, and C. The experiment coordinate system is also shown; x is the streamwise/ out-of-plane direction, y is the vertical wall-normal direction, and z is the spanwise wall-normal direction. The origin is located at the bottom right corner of the AWM

performed at velocities ranging from 16 to 32 ms^{-1}. As the length of each wind tunnel run was on the order of a minute, the cameras were assumed to have a constant position across different runs. Based on this, the adjustment of Scheimpflug angles and lens focus was performed at $U_\infty =$ 16 ms^{-1}, and calibration images were taken shortly after data collection was completed.

To provide a comparison of the calibration targets, the data from each SPIV system were processed twice in DaVis version 10.1.1.61838; once with a calibration based on a Type 31 target and once with a calibration based on the LEGO® target. For both targets, a pinhole calibration was used, and planar self-calibration was subsequently performed in order to account for the true orientation of the laser sheet. Prior to SPIV processing, a bright-field correction was applied to improve particle detection by increasing the imaged light intensity and then subtracting the average image calculated over the first 200 images of each dataset. During SPIV processing, a final interrogation

Table 1 Comparison of basic calibration parameters output by DaVis for Type 31 and LEGO® calibration targets. Data presented for FOV C

	Type 31	LEGO®
Mean fit error [px]	0.1233	0.3363
Dewarped area [mm²]	620.9 × 436.1	608.7× 430.6
Stereo angle US	33.86°	33.58°
Stereo angle DS	29.76°	33.84°

window size of 32×32 px was used with a 50% overlap; this corresponds to a physical resolution of approximately 2.5 mm.

5 Comparing calibration targets

In the interest of brevity, the comparisons presented in this paper are performed on FOV C, which captures the bottom corner of the wind tunnel, and for $U_\infty =$ 16 ms^{-1}. An initial comparison of the calibrations is based on information about the fit error, dewarped image area, and inferred stereo viewing angles provided by DaVis and is shown in Table 1. Notably, although the Type 31 target has a fit error approximately 3× lower than that of the LEGO® target, the absolute magnitude of this uncertainty is vanishingly small in physical units. At the ∼ 2.3 m working distance in this experiment, the fit error for the LEGO® target is approximately 0.052 mm. Both targets have a similar dewarped image area, with a difference of 12.2 mm and 5.5 mm in the spanwise and vertical directions, respectively. As with the fit error, this disagreement is small in comparison to the size of the FOV. This is also influenced by the planar self-calibration, which is slightly different for each calibration. For the upstream camera, the inferred stereo viewing angles are almost identical. Interestingly, this is not the case for the downstream camera, which differ by almost 4°.

Although the calibration parameters are interesting from an optics standpoint, a practical point of comparison lies in the SPIV data generated with the different calibrations. Here, all data considered are derived from the ensemble-average over the 950 images 900 images taken during each experimental run. To provide a numeric comparison of the SPIV output, the mean and median values of all three (ensemble-averaged) velocity components and their absolute deviations calculated over the FOV are tabulated in Table 2. Due to the large velocity gradients present near the wall, mean and median values for u differ somewhat regardless of the calibration target used. However, this is consistent and the good agreement between the u fields calculated is also reflected in the low mean and median u field deviation. These correspond to ~0.8%

Table 2 Comparison of FOV-based field parameters for Type 31 and LEGO® calibration targets. Here, mean and median values are calculated based on every element in the FOV. The deviation values are calculated based on every element in an interpolated FOV composed of the absolute difference of the field values generated by the Type 31 and LEGO® targets

	Type 31	LEGO®	Deviation
FOV mean u [ms^{-1}]	15.11	14.98	0.122
FOV mean v [ms^{-1}]	−0.14	−0.02	0.135
FOV mean w [ms^{-1}]	−0.27	−0.18	0.152
FOV median u [ms^{-1}]	15.88	15.81	0.083
FOV median v [ms^{-1}]	−0.15	−0.01	0.133
FOV median w [ms^{-1}]	−0.25	−0.23	0.110

and ~0.5% of the freestream velocity, respectively. At first glance, the cross-stream components v and w show significantly less agreement. However, the magnitude of the cross-stream components is far smaller than that of the out-of-plane component, making the metric somewhat misleading. In contrast, the deviation values which provide a measure of the overall disagreement between the results from both calibrations over the entire FOV are not significantly higher than those for the u-component.

The high degree of agreement in the measurement of u can be best visualised in Fig. 6. For both calibrations, the shapes of the corner vortex and other flow features are consistent and practically identical. This can be further verified by analysing the disparity between the two fields shown in Fig. 7. Contours of the relative disparity between the fields calculated using the different calibrations provide a dimensional measure of the disagreement between the results. In order to highlight regions of significant deviation, an artificial measure of normalised disparity between two scalar fields A and B was defined,
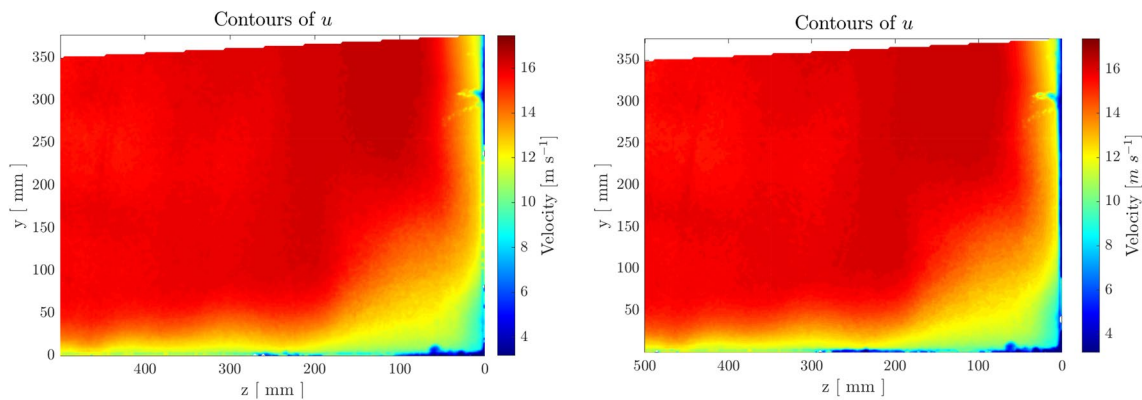

Fig. 6 Contours of u, the streamwise and out-of-plane velocity component, for FOV C obtained after SPIV processing with a Type 31 target (left) and after SPIV processing with the LEGO® target (right). Note that regions with insufficient or invalid data appear as white points
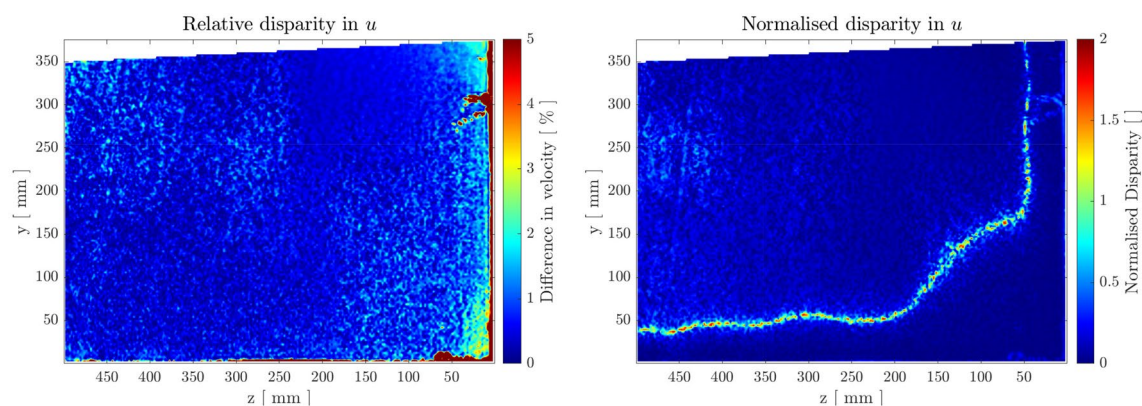

Fig. 7 Contours of relative disparity (left) and normalised disparity (right) between u fields obtained using different calibration targets. Note that the apparent disparities are likely slightly exaggerated due to minor misalignments between the datasets that are a result of their differing discretisations; the line of high normalised disparity along the edge of the boundary layer is to be expected due to the high sensitivity of that region of the flow. Note that regions with insufficient or invalid data appear as white points

$$1 - \frac{(A_{ij} - \mu_A)(B_{ij} - \mu_B)}{\max(|A_{ij} - \mu_A|, |B_{ij} - \mu_B|)^2} \qquad (2)$$

where μ_A and μ_B are the element-wise averages of A and B. Here, perfectly matching scalars at a location (i, j) would output a null value. When applied to the u component as in Fig. 7, it highlights some disagreement at the edge of the boundary layer, but shows that the disparity is low across most of the FOV.

The combination of different metrics used to compare the output from both calibration targets paints a slightly cloudy, if promising picture. The calibration parameters shown in Table 1 indicate that despite the higher mean fit error produced when using the LEGO® target, the imaged area and inferred stereo angles are comparable. When analysed in terms of mean and median values of the velocity components calculated over the FOV, the in-plane components (v, w) indicate poor quantitative agreement, with a significant departure in the magnitude of in-plane components. However, as shown in Fig. 8, there is no immediately apparent deviation in the vector angles. Notably, the core of the corner vortex, which is a useful "landmark" in the flowfield, is located at approximately $z = 115$ mm, $y = 35$ mm for both cases. Furthermore, the u field shows excellent agreement, both when analysed in terms of absolute deviation and the synthetic measure of disparity from Eq. 2. This, along with the good comparability of the calibration parameters indicates that the disagreement in the measurement of in-plane components might not be caused by the choice of calibration target. Due to the relatively large magnitude of the out-of-plane component, it is likely that short particle residence times in the laser sheet produced poor correlations for the in-plane components. Another potential source of

the disagreement could be the coarser marker pitch on the LEGO® target, which is approximately 3x greater than that of the Type 31 target.

6 Parametric evaluation of LEGO targets

In order to further investigate the discrepancies observed during the experiments, a small parametric study focussing on a variation of patterns and marker sizes on LEGO® targets was performed. Here, the experimental set-up formerly introduced was simplified to consist of a single pair of sCMOS cameras, oriented to image targets placed at a working distance and viewing angle of approximately 2.1 m and 45°, respectively. A Type 31 target was imaged and used to produce a baseline SPIV calibration using the pinhole method (Tsai 1986). A smaller LEGO target, based on 32×32 stud (approximately 25×25 cm) baseplates which were mounted on a thin MDF plate, was then imaged with a series of different patterns. The first variable modified was marker pitch; this was varied between 32 mm, 48 mm, and 64 mm. The second variable of interest was the influence of marker size on calibration. To test this, the larger 2×2 circular tiles, which have a diameter of 15.8 mm and were used for the initial intensity ratio tests, were imaged with pitches of 48 mm, 64 mm, and 96 mm. An overview of these patterns is presented in Fig. 9. In order to compare the calibration results, each individual configuration was evaluated in terms of mean fit error and reported pixel-to-real-world conversion factor, as these are the most indicative of overall calibration quality. For all the targets tested, calibration images were masked to reduce the chance of detection errors. Calibrations were also performed with masked images which were
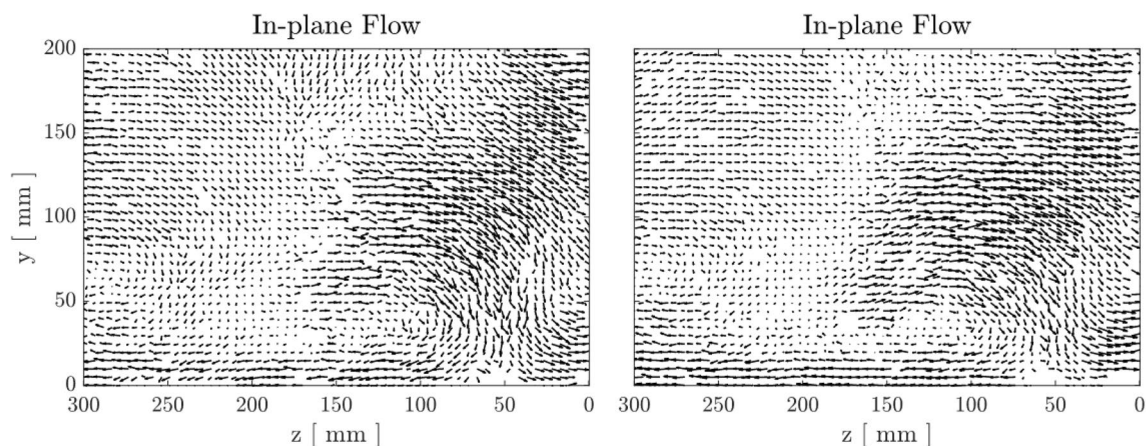

Fig. 8 Cropped views of the corner vortex obtained using calibration with a Type 31 target (left), and the LEGO® target (right). Note that the magnitudes of the in-plane components have been normalised by U_∞. Although the flowfields are not a perfect match, there is good qualitative agreement in the capture of significant flow features
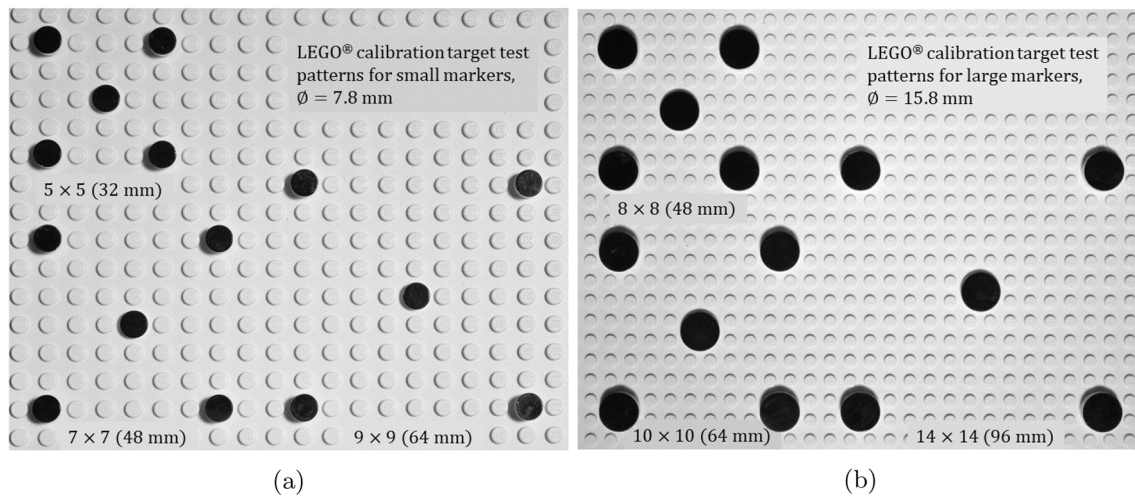
Fig. 9 LEGO® calibration patterns tested in the parametric study; patterns with small (**a**) and large markers (**b**). Note that the baseplate used was white but appears grey here due to lighting conditions

subsequently binarised using intensity-based thresholding to provide additional contrast.

The calibration process and results highlighted some interesting trends to consider when choosing a marker pattern, highlighted in Fig. 10. The first is that the LEGO® targets tended produce calibrations with a slightly higher apparent magnification, regardless of marker pitch and size, as shown in Fig. 10a. Notably, the targets with small markers had scaling factors significantly closer to that of the Type 31 target, although the use of a very sparse 64-mm pattern did result in a higher apparent magnification. The second major observation is that all of the LEGO® targets have a higher reported fit error than the Type 31 target. This result is not altogether unsurprising, given that they are hand-made and can be expected to have a lower overall precision. Furthermore, it is consistent with the initially observed differences in mean fit error; the 48-mm pitch target had a fit error approximately 2.5× that of the Type 31 target, which is comparable to the initial result reported in Table 1. The LEGO® targets with large markers have a higher fit error than those with small markers, regardless of pitch. Notably, as with the initial experiment in the AWM, the fit error remains very small when scaled. As shown in Fig. 10c, the largest scaled fit error is approximately 0.18 mm and corresponds to 4% of a 32 × 32 px interrogation window. A more typical fit error for the LEGO® targets is in the range of 0.08 mm to 0.15 mm, corresponding to ∼ 2 to 3% of an interrogation window.

From a practical target-making and usage standpoint, there were some additional trends of interest. In particular, both the 48 × 48 mm and 64 × 64 mm patterns produced lower fit error with the small markers than with the large markers, indicating that small markers are a better choice in most situations. However, for experiments involving large fields of view at low magnification, the large markers remain a potential alternative when the small markers would appear too pixelated and produce large discretisation errors in marker detection. The pattern density, or marker pitch, appears to only have a weak influence on fit error. Notably, in the tests with small markers, a small pitch of 32 mm did *not* yield a lower fit error than the pitch of 48 mm. Similarly, the marker pitches of 48 mm and 64 mm yielded almost identical fit errors for the large markers. From a practical standpoint, this means that targets with a lower overall number of markers can be made without compromising on calibration quality, reducing the labour input required. Finally, the LEGO® targets benefited from intensity-based image binarisation in most cases, with significant reductions in fit error observed in calibrations performed using binarised images. Although this is an additional step in the calibration process, it is straightforward and does not impose a great deal of additional effort on the end user.

7 Conclusion

Due to the nonintrusive nature of PIV and rapid advances in imaging and computational technology, the application of PIV and its many flavours to large-FOV measurements is highly attractive to experimentalists. One of the chief challenges encountered during the execution of these experiments is the calibration process. Namely, standard calibration targets, particularly for SPIV, tend to be somewhat small, inflexible, and expensive. This is becoming an increasingly important limitation as modern imaging and processing technology have increased the feasibility and attractiveness of large FOV experiments. To provide
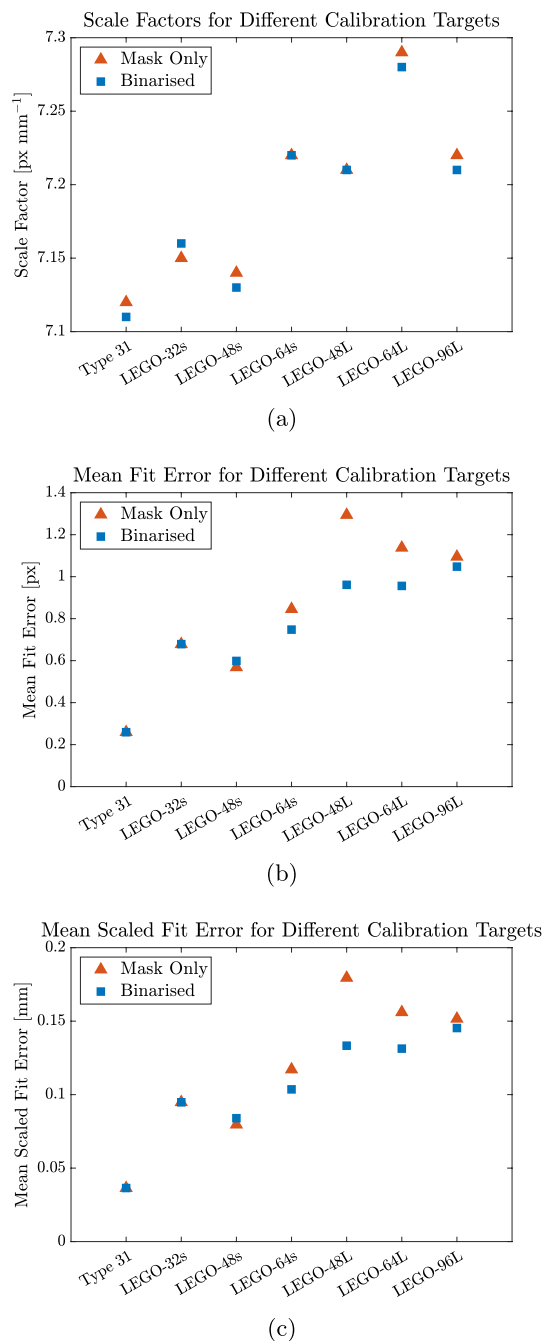
Fig. 10 Comparison of the scaling factors (**a**), mean fit errors (**b**), and scaled fit errors (**c**) produced by calibrations with the Type 31 target and LEGO® targets with small and large markers for both masked and binarised calibration images. The marker pitch, measured in mm, is added as a suffix followed by 's' or 'L' to indicate small or large markers, respectively

a solution to this problem, customised two-sided, multi-level targets were created using LEGO® bricks. With some iteration, it was possible to produce marker coatings and patterns which are readily accepted by standard PIV processing software such as DaVis in typical experimental

conditions. A large 380 × 1150 mm calibration target, consisting of three smaller modular targets, was used for SPIV measurements of the inflow conditions of the AWM. Data collected using the 6-camera SPIV set-up were then processed with calibrations performed using the LEGO® target, as well as a standard LaVision Type 31 target. Analysis of the mean field data produced showed that the LEGO® target produced results nearly identical to those generated using the Type 31 target in the streamwise, out-of-plane direction. However, the agreement for the in-plane components was not as strong. This is believed to be an artefact of the experimental set-up and the large difference in magnitudes between the out-of-plane and in-plane velocity components rather than an error intrinsic to the LEGO® calibration target itself. To further investigate the viability of LEGO®-based calibration targets as an alternative to "standard" targets and demonstrate the flexibility they offer, a parametric study of different calibration marker sizes and pattern pitches was performed. This revealed that the LEGO® targets produce calibrations with a higher fit error in a manner consistent to the results obtained observed in the initial wind tunnel tests. However, when scaled to physical units, this remains vanishingly small in terms of the experimental scales that can be observed resolved, in the range of 2 to 3% of the size of a common 32 × 32 pixel interrogation window. Binarisation of the calibration images greatly improves the performance of the LEGO® targets and is a recommended pre-processing step. The results also showed that the use of larger markers is viable and has potential for use with very large FOVs and/or low magnification experiments, such as those using helium-filled soap bubbles as tracer particles. While not presenting flawless performance, the results from both the initial experiments and the follow-up study indicate that LEGO®-based targets for large-FOV measurements present a viable low-cost and flexible alternative to more expensive and limited precision-machined targets. Beyond this, the LEGO® targets significantly simplify the experimental process and remove additional sources of error by enabling the calibration of multiple camera systems simultaneously and with the use of a single reference. To this end, in a real-world test of these benefits, the large 380 × 1150 mm calibration target was used to calibrate further measurements of the AWM cross-section, with the initial set-up being adapted to cover 3 SPIV systems imaging a FOV horizontally oriented along the floor of the tunnel. Figure 11a shows the side-by-side SPIV calibration which was successfully generated with an average fit error of 0.6420 pixels. This calibration was then applied to the raw PIV images prior to processing to produce the mean field shown in Fig. 11b, which spans an effective FOV of 350 × 1100 mm. The target covered an area of slightly more than

(a)
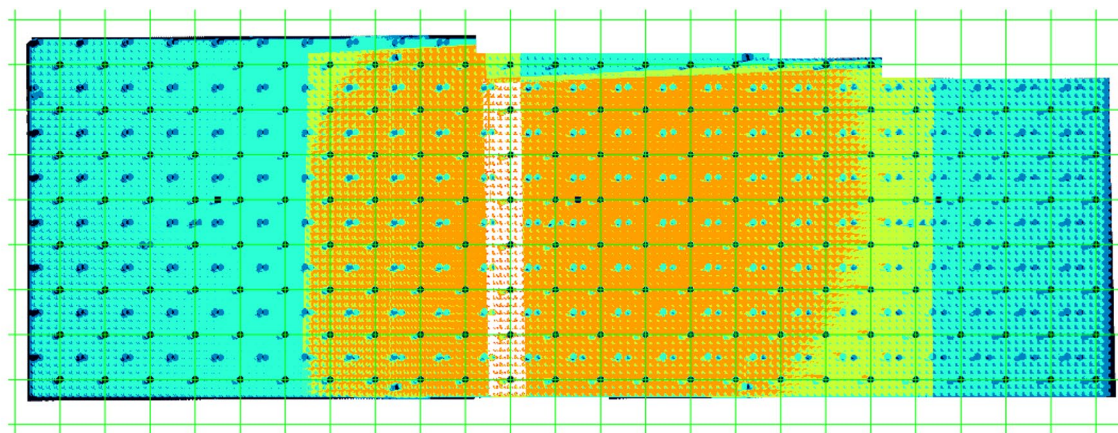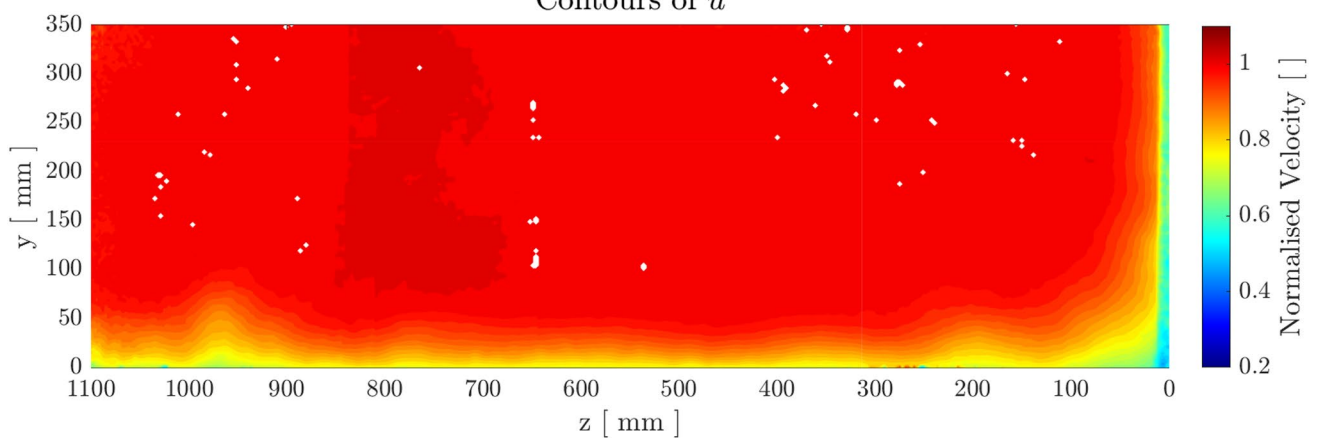
(b)

Fig. 11 Stitched calibration images (**a**) used to produce the mean-field SPIV image in (**b**). Note that the result shown in (**b**) has been cropped to include the relevant areas of interest, and that the streamwise component has been normalised by U_∞

0.4 m^2, a significant increase over the ~ 0.1 m^2 covered by the Type 31 target. This underscores the potential applicability and benefits of the LEGO® targets to the ever-larger PIV measurements being performed today.

Availability of data and materials Data, technical drawings, and further information available upon request—please contact the corresponding author.

Declarations

Ethical approval Not applicable.

Conflict of interest The authors have no competing interests to declare that are relevant to the content of this article. A version of this paper was first submitted for publishing in the proceedings of the 20th International Symposium on Application of Laser and Imaging Techniques to Fluid Mechanics.

References

Cardesa JI, Nickels TB, Dawson JR (2012) 2D PIV measurements in the near field of grid turbulence using stitched fields from multiple cameras. Exp Fluids 52:1611–1627. https://doi.org/10.1007/s00348-012-1278-4

Jenkins LN, Yao CS, Bartram SM, et al (2009) Development of a large field-of-view PIV system for rotorcraft testing in the 14-x 22-foot subsonic tunnel. https://ntrs.nasa.gov/api/citations/20090022378/downloads/20090022378.pdf?attachment=true

Li H, Zhao Y, Liu J et al (2021) Physics-based stitching of multi-FOV PIV measurements for urban wind fields. Build Environ. https://doi.org/10.1016/j.buildenv.2021.108306

McKeon BJ, Comté-Bellot G, Foss JF et al (2007) Velocity. Vorticity, and Mach Number, Springer, chap 5, pp 215–472

Raffel M, Willert CE, Scarano F, et al (2018) Particle image velocimetry, 3rd edn. Springer, https://doi.org/10.1007/978-3-319-68852-7

Sankaran A, Fuchs T, Hain R, et al (2022) Stereoscopic PIV measurements of the human thermal plume. In: Proceedings of the 20th international symposium on application of laser and imaging techniques to fluid mechanics

Scharnowski S, Kähler CJ (2020) Particle image velocimetry–classical operating rules from today's perspective. Opt Lasers Eng 135(106):185. https://doi.org/10.1016/j.optlaseng.2020.106185

The LEGO Group (2018) Fair play. https://www.lego.com/cdn/cs/legal/assets/blt1a4c9a959ce8e1cb/FairPlayBrochure.pdf

Tsai RY (1986) An efficient and accurate camera calibration technique for 3D machine vision. In: CVPR 1986

Wieneke B (2005) Stereo-PIV using self-calibration on particle images. Exp Fluids 39:267–280. https://doi.org/10.1007/s00348-005-0962-z

Authors and Affiliations

Agastya Parikh[1] · Thomas Fuchs[1] · Matthew Bross[1] · Christian J. Kähler[1]

✉ Agastya Parikh
  agastya.parikh@unibw.de

1   Institut für Strömungsmechanik und Aerodynamik, Universität der Bundeswehr München, Neubiberg, Germany